The Astrophysical Journal, 921:31 (15pp), 2021 November 1 https://doi.org/10.3847/1538-4357/ac193e

Turbulent Properties in Star-forming Molecular Clouds Down to the Sonic Scale. II. Investigating the Relation between Turbulence and Star-forming Environments in Molecular Clouds

Hyeong-Sik Yun[1], Jeong-Eun Lee[1], Neal J. Evans, II[2,3,4], Stella S. R. Offner[2], Mark H. Heyer[5], Jungyeon Cho[6], Brandt A. L. Gaches[7,8], Yao-Lun Yang[9], How-Huan Chen[2], Yunhee Choi[3], Yong-Hee Lee[1], Giseon Baek[1], Minho Choi[3], Jongsoo Kim[3], Hyunwoo Kang[3], Seokho Lee[10], and Ken'ichi Tatematsu[11,12]

[1] School of Space Research, Global Campus, Kyung Hee University, 1732 Deogyeong-daero, Giheung-gu, Yongin-si, Gyeonggi-do, 17104, Republic of Korea
hs-yun@khu.ac.kr, jeongeun.lee@khu.ac.kr
[2] Department of Astronomy, The University of Texas at Austin, 2515 Speedway, Austin, TX 78712, USA
[3] Korea Astronomy and Space Science Institute, 776, Daedeok-daero, Yuseong-gu, Daejeon, 34055, Republic of Korea
[4] Humanitas College, Global Campus, Kyung Hee University, 1732 Deogyeong-daero, Giheung-gu, Yongin-si, Gyeonggi-do, 17104, Republic of Korea
[5] Department of Astronomy, University of Massachusetts Amherst, 710 N. Pleasant Street, Amherst, MA 01003, USA
[6] Department of Astronomy and Space Science, Chungnam National University, 99, Daehak-ro Yuseong-gu, Daejeon, 34134, Republic of Korea
[7] Physikalisches Institut, Universität zu Köln, Zülpicher Straße 77, D-50937, Köln, Germany
[8] Center of Planetary Systems Habitability, The University of Texas at Austin, 2515 Speedway, Austin, TX 78712, USA
[9] Department of Astronomy, University of Virginia, Charlottesville, VA 22904-4235, USA
[10] National Astronomical Observatory of Japan, 2-21-1 Osawa, Mitaka, Tokyo 181-8588, Japan
[11] Nobeyama Radio Observatory, National Astronomical Observatory of Japan, National Institutes of Natural Sciences, 462-2 Nobeyama, Minamimaki, Minamisaku, Nagano 384-1305, Japan
[12] Department of Astronomical Science, SOKENDAI (The Graduate University for Advanced Studies), 2-21-1 Osawa, Mitaka, Tokyo 181-8588, Japan
Received 2021 April 4; revised 2021 July 26; accepted 2021 July 28; published 2021 October 28

Abstract

We investigate the effect of star formation on turbulence in the Orion A and Ophiuchus clouds using principal component analysis (PCA). We measure the properties of turbulence by applying PCA on the spectral maps in ^{13}CO, C^{18}O, HCO$^+$ $J = 1$–0, and CS $J = 2$–1. First, the scaling relations derived from PCA of the ^{13}CO maps show that the velocity difference (δv) for a given spatial scale (L) is the highest in the integral-shaped filament (ISF) and L1688, where the most active star formation occurs in the two clouds. The δv increases with the number density and total bolometric luminosity of the protostars in the subregions. Second, in the ISF and L1688 regions, the δv of C^{18}O, HCO$^+$, and CS are generally higher than that of ^{13}CO, which implies that the dense gas is more turbulent than the diffuse gas in the star-forming regions; stars form in dense gas, and dynamical activities associated with star formation, such as jets and outflows, can provide energy into the surrounding gas to enhance turbulent motions.

Unified Astronomy Thesaurus concepts: Interstellar medium (847)

1. Introduction

Turbulence is a ubiquitous phenomenon in the interstellar medium and plays a crucial role in the evolution of molecular clouds (MCs; Mac Low 2003; Elmegreen & Scalo 2004). A large-scale turbulent motion with a supersonic speed produces shocks that make density and velocity fluctuations in MCs. Within these fluctuations, high-density regions evolve to clumps and cores via gravitational collapse (Padoan et al. 2001; Klessen 2004; Mac Low & Klessen 2004). On the other hand, large-scale supersonic turbulence can also prevent global collapse and support the structure of MCs (Klessen 2004; Mac Low & Klessen 2004; Federrath 2015). On small scales, the fragmentation of dense cores is also affected by turbulence (Walch et al. 2012), and stars are actively formed after the dissipation of turbulence (Myers 1983; Goodman et al. 1998; Nakano 1998).

Turbulence is known to be one of the essential factors determining the star formation rate (SFR) in the interstellar medium (Federrath & Klessen 2012; Federrath 2015, 2018). Federrath (2015) showed that turbulence, as well as magnetic fields and stellar feedback, should be included in numerical simulations to produce a realistic SFR. The SFR depends on how the turbulence energy is distributed between the compressive and solenoidal modes; the SFR is enhanced more by the compressive mode than the solenoidal mode (Federrath & Klessen 2012; Federrath 2018). As a result, turbulence influences when and where stars form (McKee & Ostriker 2007; Hennebelle & Falgarone 2012; Padoan et al. 2014), and understanding the nature of turbulence is important to better understand the star formation in the interstellar medium.

After Larson (1981) found the power-law relation between the line width and size of MCs, many studies have investigated the line width-size relations for MCs (Solomon et al. 1987; Heyer et al. 2009) and cores (Myers 1983; Goodman et al. 1998) using various molecular lines. The power-law indices of the line width-size relations have been compared with that of the velocity spectrum of turbulence to study a common feature of interstellar turbulent motion. Goodman et al. (1998) introduced four types of the line width-size relations (Types 1–4). These relations may have different slopes, and thus, provide information on different characteristics of interstellar turbulence. Among these types, the Type 4 relation obtained for a single tracer for a single cloud is probably the best diagnostic tool of the turbulence within a cloud (Goodman et al. 1998).

Turbulence is statistically characterized by the way kinetic energy varies with a wavenumber (k) in Fourier space (i.e., energy spectrum $E(k) \propto k^{-\beta}$; Kolmogorov 1941). For

example, incompressible subsonic turbulence gives $\beta = 5/3$ (Kolmogorov 1941), while supersonic compressible turbulence gives $\beta = 2$ (Passot et al. 1988; Gammie & Ostriker 1996). Unfortunately, obtaining an energy spectrum from molecular line maps is challenging (Elmegreen & Scalo 2004). One approach to obtain the properties of turbulence is measuring the velocity structure function using statistical methods (Heyer & Schloerb 1997; Klessen 2000; Ossenkopf & Mac Low 2002; Elmegreen & Scalo 2004; Boyden et al. 2018; Xu 2020). The 2nd order velocity structure function is related to the autocorrelation function, which in turn is the inverse Fourier transform of the power spectrum. Within the inertial range, the structure function follows a power-law relationship with spatial displacement, l,

$$\sqrt{\langle v_l^2 \rangle} \propto l^{\gamma}. \quad (1)$$

A typically relation between the exponents γ and β is $\gamma = (\beta - 1)/2$. A recent study using a high-resolution simulation (Federrath et al. 2021) showed that β for subsonic and supersonic turbulence are 0.39 ± 0.02 and 0.49 ± 0.01, respectively, which are consistent with other theoretical studies (Kolmogorov 1941; Passot et al. 1988; Gammie & Ostriker 1996).

Principal component analysis (PCA; Heyer & Schloerb 1997; Brunt & Heyer 2013) is one of the statistical methods to derive the underlying low order velocity structure function of turbulence from an observed spectral map (Heyer & Schloerb 1997; Brunt & Heyer 2002a; Brunt et al. 2003; Heyer & Brunt 2004; Heyer et al. 2009; Roman-Duval et al. 2011; Feddersen et al. 2019). PCA utilizes both spatial and velocity information and derives the power-law relation between a velocity difference (δv) and spatial scale (L) of turbulent motions,

$$\delta v = \delta v_0 L^{\alpha}, \quad (2)$$

where δv_0 is δv at 1 pc, and α is a PCA scaling exponent. The PCA scaling exponent is rescaled to γ based on the calibration described by Brunt & Heyer (2002b) and Brunt et al. (2003). We refer to this power-law relation as a scaling relation of PCA. The scaling relation is considered to be one of the Type 4 relations because it describes variation of velocity difference traced by a single molecular line as a function of spatial scale within a cloud.

Using PCA, Heyer & Brunt (2004) derived the scaling relation from the spectral map of ^{12}CO $J = 1$–0 for each of 27 giant MCs. They found that the α and δv_0 values for 27 MCs are all similar each other (α and δv_0 are 0.62 ± 0.09 and $0.90 \pm 0.9\,\mathrm{km\,s^{-1}}$, respectively). This mean value of α corresponds to a mean value of $\gamma = 0.51$. The small scatter in α and δv_0 for this set of clouds strongly suggests that the velocity structure functions derived over the full extent of MCs follow the same functional form, indicating that turbulence is universal in the molecular interstellar medium. However, Heyer et al. (2006) also found that the derived δv_0 values can vary with the local environment within a molecular cloud. This δv_0 difference could be related to the local energy dissipation or injection within the cloud such as stellar feedback from star-forming activities (Boyden et al. 2016). Koch et al. (2017) carried out a systematic parameter study of MCs using magnetohydrodynamic simulations and found PCA is also sensitive to changes in the virial, plasma parameters, and the solenoidal fraction of the turbulence.

Other factors that can cause the δv difference for a given L is the uncertainty of distance (Heyer & Brunt 2004). PCA derives each L via multiplying the angular size of turbulent motion by the distance to a cloud. If the distance is overestimated, PCA would overestimate L and consequently underestimate δv for a given L. Uncertain distances to MCs therefore cause the over and underestimation of L, resulting in a difference in δv between the MCs. Therefore, knowing the accurate distance is important for investigating the turbulence scaling relation correctly.

Many previous studies of turbulence have observed the $J = 1$–0 transition of the ^{12}CO and ^{13}CO molecules (Bally et al. 1987; Heyer et al. 1992; Nagahama et al. 1998; Shimajiri et al. 2011; Kong et al. 2018), which are the main tracers of molecular gas. But they can often fail to trace the entirety of the gas motions due to their optical thickness. Since cores and stars form in dense environments (Padoan et al. 2001; Mac Low & Klessen 2004), measuring turbulence in the dense parts of clouds is important to understand the relation between turbulence and star formation. Therefore, sampling MCs using multiple molecular transitions, which can trace different density environments, is necessary to investigate the properties of turbulence in the whole cloud (Gaches et al. 2015). This multi-transition study of a cloud can derive the Type 3 relation of Goodman et al. (1998), which is associated with various density environments. By comparing the Type 3 relations between the MCs that have different star-forming environments, a relation between turbulence and star formation can be investigated (the Type 1 relation of Goodman et al. 1998).

To assess the relation between turbulence and star formation, we carried out a systematic observation program for the Orion A and Ophiuchus clouds (Yun et al. 2021, Paper I) using the Taeduk Radio Astronomy Observatory (TRAO) 13.7 m telescope (Roh & Jung 1999; Jeong et al. 2019). The TRAO telescope is an excellent facility to observe large areas in multiple molecular transitions efficiently. The Orion A and Ophiuchus clouds contain various star-forming environments: active massive and low-mass star formation occurs in the Orion A cloud (Ikeda et al. 2007; Allen & Davis 2008; Megeath et al. 2012; Nakamura et al. 2012; Furlan et al. 2016), and active low-mass star formation occurs in the Ophiuchus cloud (Motte et al. 1998; Wilking et al. 2008; Zhang & Wang 2009; Dunham et al. 2015). We observed these clouds in six molecular lines that trace different density environments. All the data were obtained via the TRAO Key Science Program (TRAO-KSP), mapping "Turbulent properties In star-forming MolEcular clouds down to the Sonic scale" (TIMES; PI: J.-E. Lee; Paper I).

In this paper, we analyze the spectral maps obtained toward the Orion A and Ophiuchus clouds using PCA and investigate the scaling relations. We summarize the observed data in Section 2. Section 3 describes a methodology of PCA and the effect of a noise distribution on the PCA results. The results of PCA from the observed data are presented in Section 4. In Section 5, we will assess how the PCA results are related to the star formation activities and large-scale motion of the observed clouds. Section 6 summarizes the results of this paper.

2. Observations

We observed the Orion A and Ophiuchus clouds in six different molecular lines. The recent studies of distance using the Gaia DR2 data reveal the detailed distance to the Orion A

Table 1
Distance to the Orion A Cloud

l Bin[a] (degree)	$\bar{d}_{\rm YSOs}$[a] (pc)	$\bar{d}_{\rm Reg}$[b] (pc)
ISF		
208.0–209.0	391 ± 24	
208.5–209.5	393 ± 25	392
209.0–210.0	393 ± 22	
Tail-N		
209.5–210.5	390 ± 26	
210.0–211.0	395 ± 30	
		399
210.5–211.5	401 ± 30	
211.0–212.0	409 ± 32	
Tail-S		
211.5–212.5	417 ± 44	
212.0–213.0	423 ± 46	
		431
212.5–213.5	435 ± 36	
213.0–214.0	448 ± 32	
L1647-S		
213.5–214.5	461 ± 40	
		464
214.0–215.0	467 ± 38	

Notes.
[a] From Großschedl et al. (2018).
[b] The arithmetic mean of the $\bar{d}_{\rm YSOs}$ values within each subregion.

(Großschedl et al. 2018) and Ophiuchus clouds (Zucker et al. 2019). The distance to the Orion A cloud varies from 391–467 pc along the filamentary structure (see Table 1; Großschedl et al. 2018). Meanwhile, Zucker et al. (2019) found a relatively constant distance across the Ophiuchus cloud, 144 ± 7 pc on average. This distance value is consistent with the distances to L1688 and L1689, which were measured using Very Long Baseline Array parallax measurements (Ortiz-León et al. 2017). We thus adopt the distance to L1688 from Ortiz-León et al. (2017), 137 ± 1 pc, because of its small uncertainty. These detailed determinations of distances make the Orion A and Ophiuchus clouds ideal targets to precisely assess the relation between turbulence and star formation environments.

The observation is carried out using the TRAO 13.7 m radio telescope as the TRAO-KSP, TIMES (Paper I). The TRAO telescope has the SEQUOIA-TRAO receiver, which has 16 beams arranged in a 4 × 4 array. The accessible frequency range is from 85–115 GHz with a fine spectral resolution of about 15 kHz resulting in a velocity resolution of 0.04 km s^{-1} at 110 GHz. The beam size is 46″ at 110 GHz. Also, SEQUOIA-TRAO allows access to two lines at 85 −100 GHz or 100−115 GHz, simultaneously (Jeong et al. 2019).

All the spectral maps were obtained using the on-the-fly mapping technique, which is efficient for observing a large area. We observed the MCs with not only ^{13}CO $J = 1$–0 but also C^{18}O $J = 1$–0, HCN $J = 1$–0, HCO$^+$ $J = 1$–0, N_2H^+ $J = 1$–0, and CS $J = 2$–1, which trace gas in different density environments (Gaches et al. 2015). The pixel size and velocity resolution of the spectral maps are 20″ and 0.1 km s^{-1}, respectively. All the spectral maps were obtained between 2016 and 2019. The details of the observation sequence and observed data were presented in Paper I.

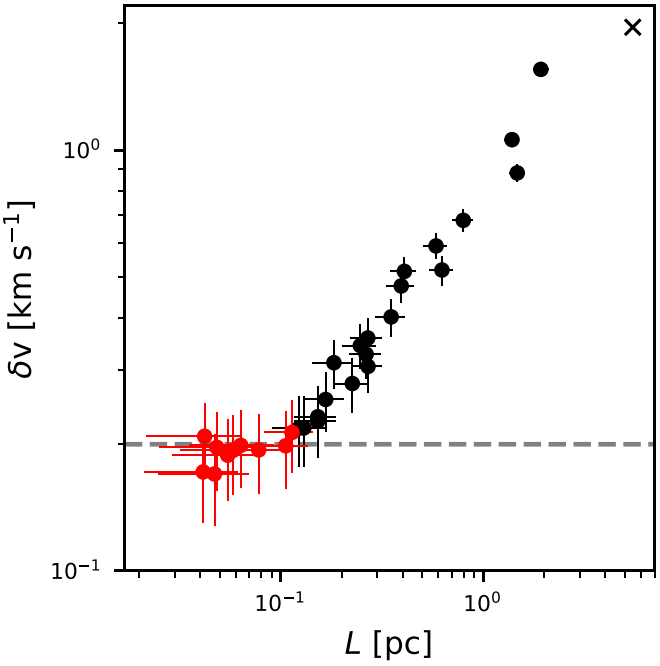

Figure 1. An example of the PCA result for the ^{13}CO line in the Orion A cloud. The black cross represents the (δv, L) point for the 2nd PC, and the black circles represent those from the 3rd to the 22nd PCs. The (δv, L) points from the 23rd to the 32nd PCs are marked with the red circles. The gray dashed line indicates δv of 0.2 km s^{-1}, and the error bars show the 1σ error ranges. Note that the (δv, L) points of the 1st PC is omitted.

3. PCA

To measure the properties of turbulence, we analyzed each of the observed spectral maps using PCA (Heyer & Schloerb 1997; Brunt & Heyer 2013). PCA is one of the multivariate analysis methods. Its formal role is describing multidimensional data as the linear combination of orthogonal principal components (PCs), where the PCs represent the most common features of the variation of the data. The eigenvectors generated by PCA provide a measure of velocity differences, δv, between observed line profiles in the map. For a given PC, the eigenimage, which is the dot product of each spectrum with the eigenvector, convey the spatial scale (L) over which the velocity difference occurs. The statistical error of this projection for a given position is equal to the rms of the spectrum.

The PCA produces $N_{\rm chan}$ orthogonal PCs, where $N_{\rm chan}$ is the number of velocity channels in the cube data. From the PCs produced by the PCA, we have to consider only significant PCs in our further analysis. Figure 1 shows an example of the PCA for the ^{13}CO line in the Orion A cloud; the (δv, L) points for the PCs up to the 32nd order are presented. Higher-order PCs represent increasingly smaller velocity differences that occur at increasingly smaller spatial scales in the cloud. If the eigenprojection values are indistinguishable from noise fluctuations, the measured velocity difference converge to a constant value (the red symbols in Figure 1). Also, noisy patterns appear on their corresponding eigenimages (see the Appendix). Therefore, we adopt only the PCs (the black symbols) up to the order that starts to be insignificant or dominated by the noise. More discussion on how to select significant PCs are discussed in the Appendix. The percentage of variation ($p_{\rm var}$), which describes the fraction of the total variation covered by

Table 2
Parameters for the TRAO and FCRAO Data

Data	Line	Beam Size ($''$)	Pixel Size ($''$)	Velocity Resolution (km s^{-1})	$T_{\rm rms}$ (K)
TRAO data	^{13}CO $J = 1$–0	46	20	0.084	0.228 ± 0.021
FCRAO data	^{13}CO $J = 1$–0	46	23	0.066	0.244 ± 0.058

the adopted significant PCs, is defined by

$$p_{\rm var} = 100\frac{\sum_{i=1}^{N_{\rm sig}}\lambda_i}{\sum_{i=1}^{N_{\rm chan}}\lambda_i}, \quad (3)$$

where $N_{\rm sig}$ is the number of significant PCs and λ_i is an ith eigenvalue.

Among the significant PCs, the first-order (1st) PC reflects variance from spectral channels with signal against those spectral channels with only noise. Following Brunt & Heyer (2002a), we thus omit the 1st PC. Also, the (δv, L) point of this component is often displaced from the best-fit power-law relation. The 2nd PC describes the largest velocity difference with the largest size. Therefore, this component often describes a large-scale systematic variation of velocity, such as the NW-SE velocity gradient in the Orion A cloud (Heyer et al. 1992; Tatematsu et al. 1993; Shimajiri et al. 2011; Kong et al. 2018). In this case, we also exclude the (δv, L) point of the 2nd PC from the fit to avoid any probable contamination by the large-scale systematic motion.

The resulting (δv, L) points generally follow a power-law relation ($\delta v = \delta v_0 L^{\alpha}$; a scaling relation). Refer to Heyer & Schloerb (1997) and Brunt & Heyer (2013) for more details of the methodology of PCA. In this paper, the best-fit δv_0, α, and their uncertainties for each of the scaling relations were estimated via the bootstrapping method with an orthogonal distance regression technique.

PCA results are generally unaffected by variations of pixel size and velocity resolution (Brunt & Heyer 2002b) but can be impacted by the level and inhomogeneity of the noise as differences in line profiles become indistinguishable from those generated by noise. We tested the effect of inhomogeneous noise on the PCA results by comparing our TRAO data set with prior observations having different noise properties. We adopted the ^{13}CO data for the L1688 region in the Ophiuchus cloud obtained using the Five College Radio Astronomy Observatory (FCRAO) telescope as part of the Coordinated Molecular Probe Line Extinction and Thermal Emission Survey (Ridge et al. 2006). Table 2 shows the parameters of the TRAO and FCRAO data, such as the beam size, pixel size, velocity resolution, and rms noise temperature ($T_{\rm rms}$). The mean $T_{\rm rms}$ values for both data are similar. However, Figure 2 shows that the probability distribution function (PDF) of $T_{\rm rms}$ for the FCRAO data is skewed to higher values, while that of the TRAO data shows a Gaussian-like distribution.

We assess the effect of the noise distribution on the PCA results by comparing the scaling relations for the TRAO and FCRAO data. The bottom panel of Figure 2 shows the PCA scaling relations for the ^{13}CO data obtained with the two radio antennae. The best-fit α and $\log(\delta v_0)$ values for the FCRAO data are consistent with those of the TRAO data within a 1σ range. Meanwhile, the eigenimage of the TRAO data exhibits the noisy pattern in a higher-order PC (the 13th PC) compared to that of the FCRAO data (the 11th PC) resulting in different $N_{\rm sig}$: the PCA analysis found 11 PCs from the TRAO data,

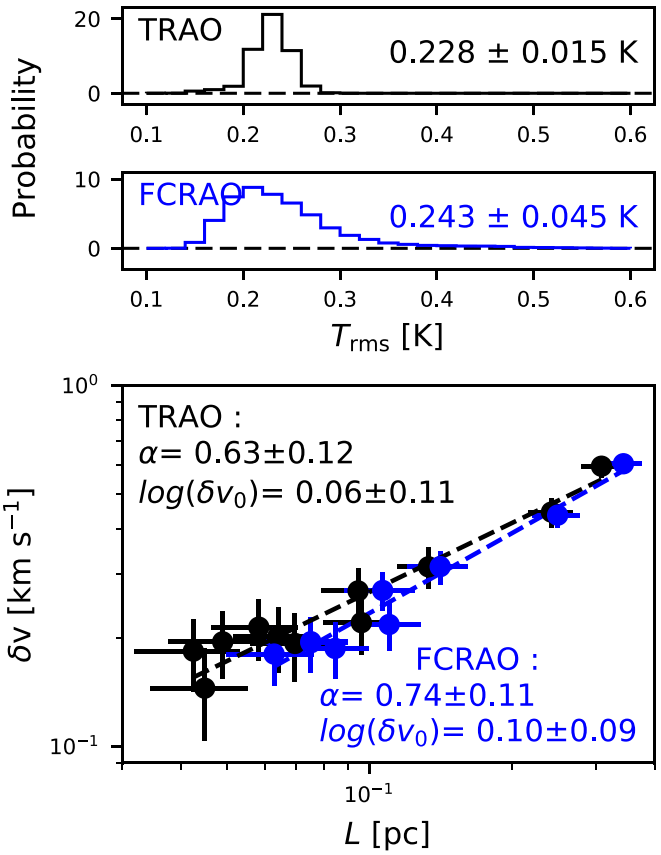

Figure 2. The two PDFs of the noise temperature ($T_{\rm rms}$) for the ^{13}CO lines in the L1688 region, which were obtained using the TRAO telescope and the FCRAO telescope (Ridge et al. 2006), are presented in the top and middle panels, respectively. The PCA scaling relations for the ^{13}CO maps are shown in the bottom panel. The δv, L pairs derived from the eigenvectors and eigenimages for the TRAO and FCRAO data are represented by the black and blue circles, respectively. The error bars indicate a 1σ error. The power-law fitting result for each scaling relation is represented by the dashed line. The best-fit α and $\log(\delta v_0)$ values are summarized at the corners.

while it found nine PCs from the FCRAO data. As a result, with these PCs, $p_{\rm var}$ for the TRAO data ($p_{\rm var} = 98.2\%$) is higher than that for the FCRAO data (97.4%). More significant PCs allow one to assess the δv in a smaller L.

4. Results

4.1. PCA Results for ^{13}CO J = 1–0

We applied the PCA method to the ^{13}CO map of the Orion A and Ophiuchus clouds. The distance to the Orion A cloud is assumed as the average distance of 416.3 pc over the cloud (Kounkel et al. 2018, see Section 5.4 in Paper I). Figure 3 shows the scaling relations for ^{13}CO in the Orion A and Ophiuchus clouds. Table 3 shows $N_{\rm sig}$, $p_{\rm var}$, and the best-fit δv_0 and α for the PCA of both clouds. The γ values corresponding to the best-fit α values are 0.56 and 0.34 for the Orion A and

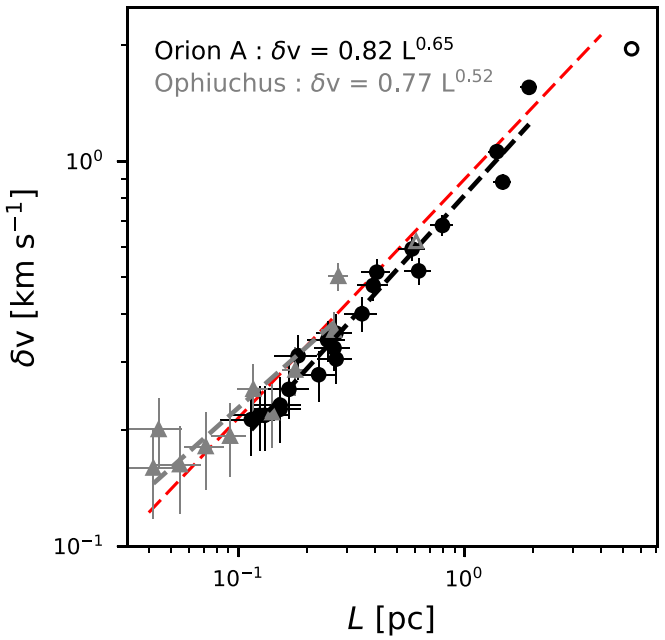

Figure 3. The scaling relations for the ^{13}CO line in the observed entire clouds. The black circles and gray triangles indicate the PCs of the Orion A and Ophiuchus clouds, respectively. The open symbols represent the 2nd PCs that are not considered in the fitting process. The best-fit power-law relations are represented by the dashed lines and summarized on the upper-left corner. The scaling relation of the universality of turbulence (Heyer & Brunt 2004) is represented by the red dashed line.

Table 3
The PCA Results for the ^{13}CO Line for Each Cloud

Cloud	N_{sig}	p_{var}	$\log_{10}(\delta v_0)$	α
Orion A	22	72.1	-0.09 ± 0.02	0.65 ± 0.05
Ophiuchus	12	90.3	-0.12 ± 0.13	0.52 ± 0.14

Ophiuchus clouds, respectively. The set of δv, L values lie close to the universal relationship (the red dashed line in Figure 3) derived by Heyer & Brunt (2004).

The p_{var} for the Orion A cloud is lower than that for the Ophiuchus cloud (see Table 3). The ^{13}CO map of the Orion A cloud has a wider velocity coverage (from -20 to 40 km s^{-1}) than that for the Ophiuchus cloud (from -7 to 14 km s^{-1}; Paper I), including the velocity gradient along the Orion A filament. Therefore, a large portion of the cube data in the Orion A cloud is filled with channels dominated by noise, resulting in a greater contribution of noise to the total variation. The p_{var} value also varies with the total integrated intensity of the molecular line in the data. For example, the HCO$^+$ and CS lines in L1688 of the Ophiuchus cloud are weaker than those in the integral-shaped filament (ISF) of the Orion A cloud (Paper I), resulting in much lower p_{var} values (see Section 4.2).

Adopting a single distance to the Orion A cloud would cause an over or underestimation of δv at a given L; for example, if we adopt 416.3 pc, instead of 470 pc, for the distance to L1647-S (Großschedl et al. 2018), L would be underestimated resulting in an overestimation of δv for a given L. Also, star formation environments vary depending on the position within the MC (Ikeda et al. 2007; Allen & Davis 2008; Nakamura et al. 2012; Dunham et al. 2015). Therefore, we divide the

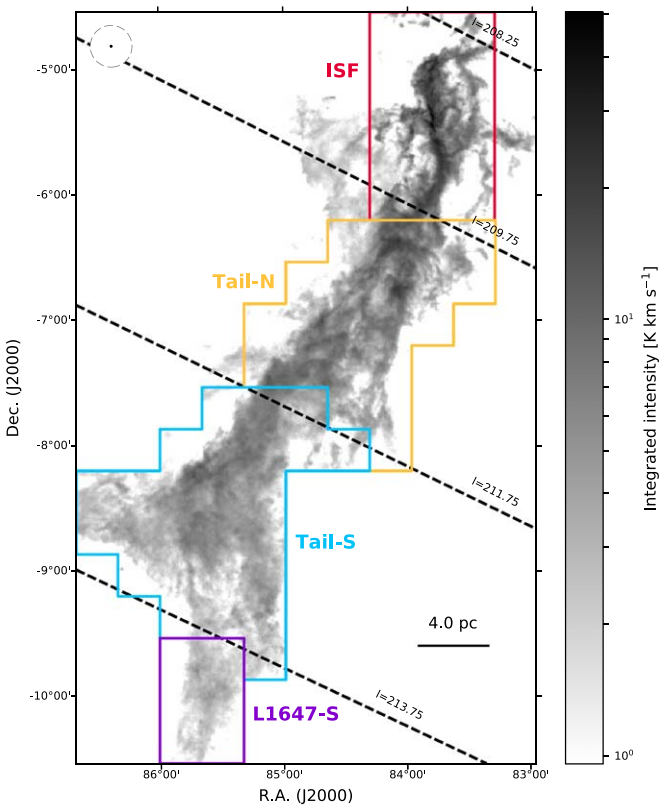

Figure 4. Four subregions selected based on the distances listed in Table 1. Four selected subregions are outlined with solid lines in different colors. The black dashed lines indicate the edges of the selected subregions in galactic longitude. Because the ranges of l for the subregions are overlapped each other (0.5°; see Table 1), we adopted l for the middle of the overlapped ranges ($l = 208.25°$, 209.75°, 211.75°, and 213.75°) as the edges of the subregions. The background image is the integrated intensity map of the ^{13}CO line. The black dot in the gray dashed circle on the left-upper corner is the beam size.

Orion A and Ophiuchus clouds into several subregions and investigated the PCA scaling relations of ^{13}CO.

The Orion A cloud map is divided by galactic longitude, l, of 208.25°, 209.75°, 211.75, and 213.75°. From the north to the south, the subregions are referred to as the ISF, Tail-N, Tail-S, and L1647-S regions, respectively (see Figure 4). Table 1 shows an average distance to each subregion. We also divide the Ophiuchus cloud map into two representative subregions, the L1688 and L1709 regions, which are two distinct parts with different system velocities (Loren 1989). Figure 5 exhibits the subregions in the Ophiuchus cloud. We adopt the same distance to these subregions as we adopt for the full cloud (137 pc; Ortiz-León et al. 2017).

The scaling relations for the subregions within the Orion A and Ophiuchus clouds are presented in the left and right panels of Figure 6, respectively. The N_{sig}, p_{var}, best-fit δv_0 and α values are summarized in Table 4. The scaling relations for the entire Orion A and Ophiuchus clouds are also overlaid in each panel. The scaling relations for the subregions have different δv values for a given L, where the relation for the entire cloud seems to be an average of those for the subregions (Brunt 1999). PCA results for the Orion A cloud show that the δv for a given L from the northern subregion tends to be greater than that for the southern subregion. The best-fit α values for the subregions are similar to each other ($\sim$0.7) except that for the ISF region. The ISF region has the largest δv for a given L and the highest

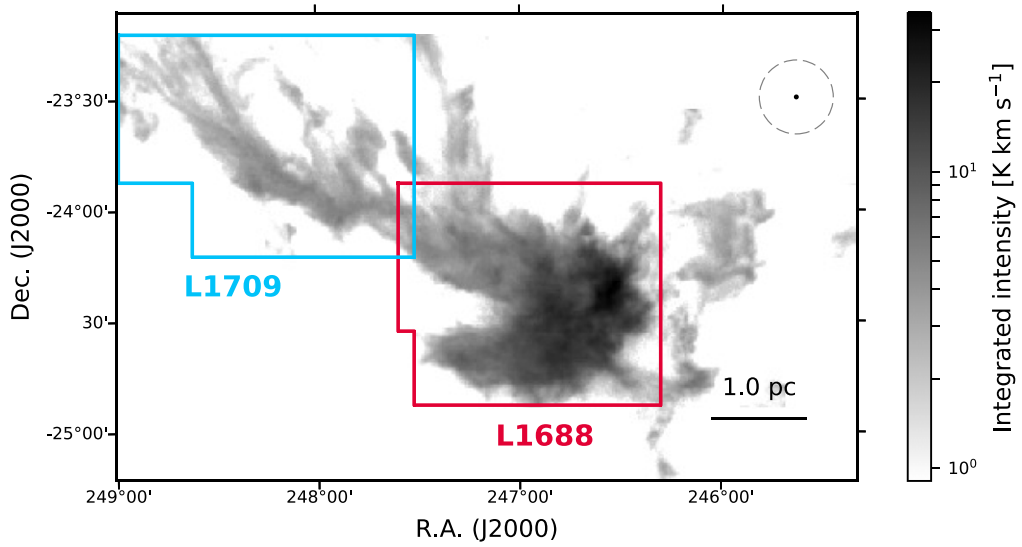

Figure 5. Two selected subregions in the Ophiuchus cloud. The background image is the integrated intensity map of the ^{13}CO line. The black dot in the gray dashed circle on the right-upper corner is the beam size.

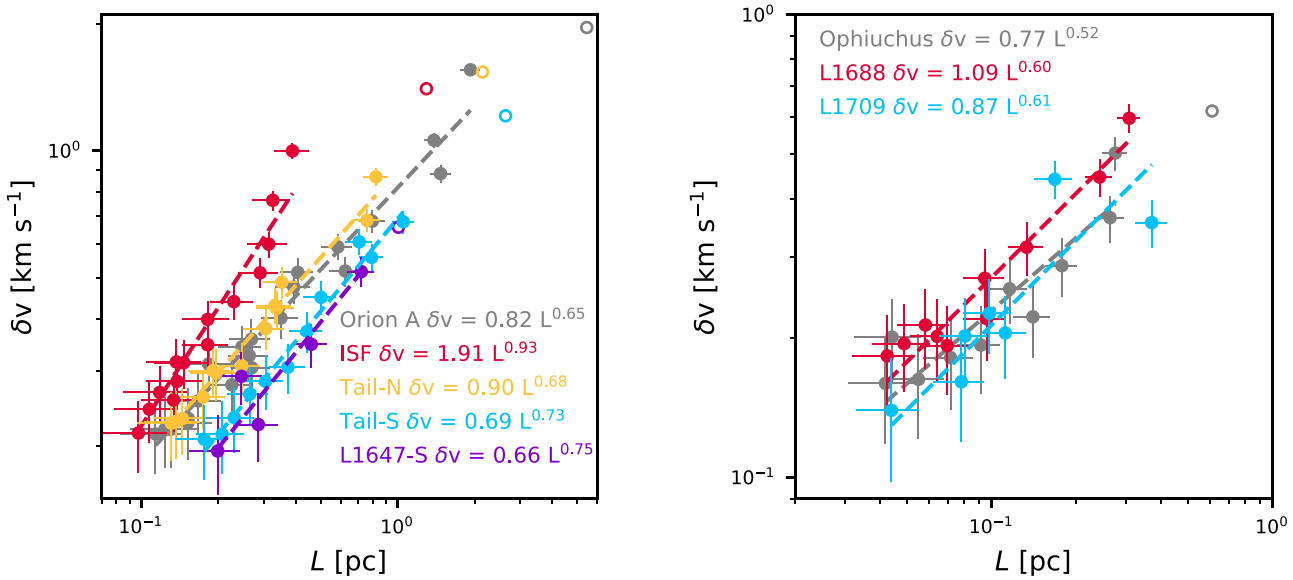

Figure 6. The scaling relations for the ^{13}CO line in the subregions of the Orion A (left) and Ophiuchus (right) clouds. The best-fit power-law relations are exhibited by the dashed lines. In each panel, the scaling relation for the entire cloud is represented in gray.

Table 4
The PCA Results for the Subregions

Region	N_{sig}	p_{var}	$\log_{10}(\delta v_0)$	α
In the Orion A cloud				
ISF	16	84.3	0.282 ± 0.124	0.933 ± 0.182
Tail-N	15	75.5	-0.047 ± 0.046	0.684 ± 0.096
Tail-S	13	63.8	-0.161 ± 0.037	0.731 ± 0.112
L1647-S	7	35.4	-0.181 ± 0.103	0.747 ± 0.249
In the Ophiuchus cloud				
L1688	11	96.5	0.036 ± 0.097	0.604 ± 0.109
L1709	8	72.6	-0.062 ± 0.191	0.609 ± 0.219

α value of 0.93. In the Ophiuchus cloud, the δv for a given L for the L1688 region is higher than that for the L1709 region. The difference in δv in the Ophiuchus cloud is relatively smaller than that in the Orion A cloud.

4.2. PCA Results for Different Density Tracers

The ISF and L1688 regions are the most active star-forming regions in the Orion A and Ophiuchus clouds, respectively. Also, the observed molecular lines in these regions are strong enough to provide good signal-to-noise ratios (Paper I). The active star formation and high signal-to-noise ratios of the observed lines make the ISF and L1688 regions ideal to study the relationship between turbulence and star formation. We thus apply PCA to the observed line maps, which trace different density environments, toward the ISF and L1688 regions. Among the observed lines, the HCN and N_2H^+ lines have hyperfine components. PCA can consider these hyperfine components as different velocity components of a cloud. Therefore, only the ^{13}CO, C^{18}O, HCO$^+$, and CS lines are used for the PCA analyses.

Figure 7 shows the scaling relations for the observed lines in the ISF and L1688 regions. The N_{sig}, p_{var}, and power-law fits

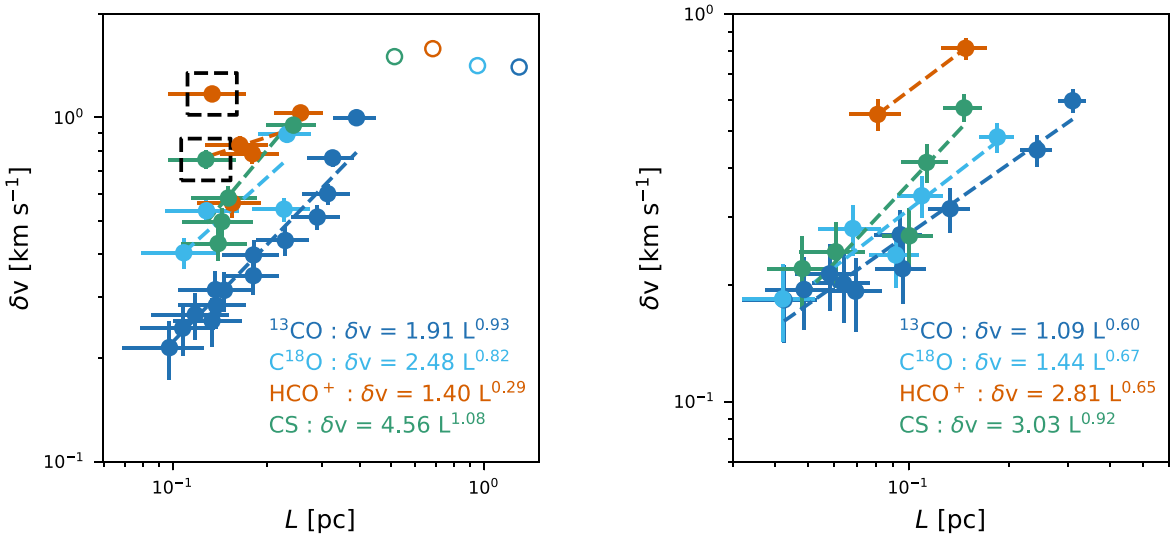

Figure 7. The scaling relations for the ^{13}CO, C^{18}O, HCO$^+$, and CS lines in the ISF (left panel) and L1688 (right panel) regions. The black dashed boxes in the left panel indicate the 6th PC of the HCO$^+$ line and the 4th PC of the CS line.

Table 5
The PCA Results for the Observed Lines

	The ISF				L1688			
Line	N_{sig}	p_{var}	$\log_{10}(\delta v_0)$	α	N_{sig}	p_{var}	$\log_{10}(\delta v_0)$	α
^{13}CO	16	84.3	0.281 ± 0.122	0.932 ± 0.179	11	96.5	0.036 ± 0.099	0.604 ± 0.111
C^{18}O	6	6.9	0.374 ± 2.198	0.788 ± 2.755	6	43.0	0.159 ± 0.232	0.665 ± 0.238
HCO$^+$	7	21.7	0.161 ± 5.494	0.311 ± 7.348	3	8.8	0.450[a]	0.650[a]
CS	7	55.7	0.685 ± 4.957	1.110 ± 6.165	6	45.5	0.481 ± 0.593	0.920 ± 0.574

Note.
[a] For the HCO$^+$ line in the L1688 region, only two PCs are used to fit a power-law relation so that there is no estimated error.

are summarized in Table 5. The scaling relations for ^{13}CO are identical to those presented in Figure 6. Except for the ^{13}CO line, the observed lines show only a few PCs, which are highly scattered within a narrow range of L in Figure 7, resulting in large uncertainties in the α and δv_0 values.

The scaling relations for C^{18}O, HCO$^+$, and CS have higher δv values for a given L compared to that of ^{13}CO. In the Orion A cloud, the scaling relations for C^{18}O, HCO$^+$, and CS are clearly separate from that of ^{13}CO. For the HCO$^+$ and CS lines, there is one PC that has an even higher δv and departs from the power-law trends expected from the other components: one is the 6th PC of HCO$^+$ and the other is the 4th PC of CS. These PCs are marked with the black dashed boxes in the left panel of Figure 7. We discuss these components in more detail in Section 5.2. In the Ophiuchus cloud, the δv values at a given L for C^{18}O and CS are slightly higher than that of ^{13}CO. The PCA result from the HCO$^+$ map clearly shows a higher δv for a given L, compared to the result from the ^{13}CO map.

5. Discussion

In this section, we investigate how scaling relations can be affected by star formation activity. We focus on the results for the Orion A cloud since it has both massive (Ikeda et al. 2007; Nakamura et al. 2012) and low-mass (Allen & Davis 2008) star-forming environments, and the scaling relations show the distinctively large δv differences (the left panels of Figures 6 and 7).

5.1. Difference in δv at a Given L

Heyer et al. (2006) found a difference in δv_0 between the subregions within the Rosette molecular cloud. They suggested that the interaction between the H II region and surrounding clouds may inject energy and increase δv_0. This result implies that δv can be affected by star formation activities within the subregions.

The left panel of Figure 6 shows that the δv at a given L decreases toward the southern part of the Orion A cloud, which is suggestive of effects of dynamical conditions. In Orion A, massive star formation occurs in the northern part (Grellmann et al. 2013), while only low-mass star formation occurs in the southern part (Allen & Davis 2008). We explore the relation between star formation activity and δv difference in more detail using the number density of Class 0/I young stellar objects (YSOs) and flat-spectrum sources (embedded protostars).

For this analysis, we adopted the catalog of embedded protostars identified with Herschel (Furlan et al. 2016) and Spitzer space telescope (Megeath et al. 2012) observations. Figure 8 presents the distribution of protostars in the Orion A cloud. Table 6 shows the number (N_{YSO}), number densities (n_{YSO}), and total bolometric luminosity (L_{bol}) of the embedded protostars in each subregion. The protostellar number density decreases from the ISF to the Tail-S region, and the values in the L1647-S and Tail-S regions are similar. This trend resembles the δv difference between the subregions. The total

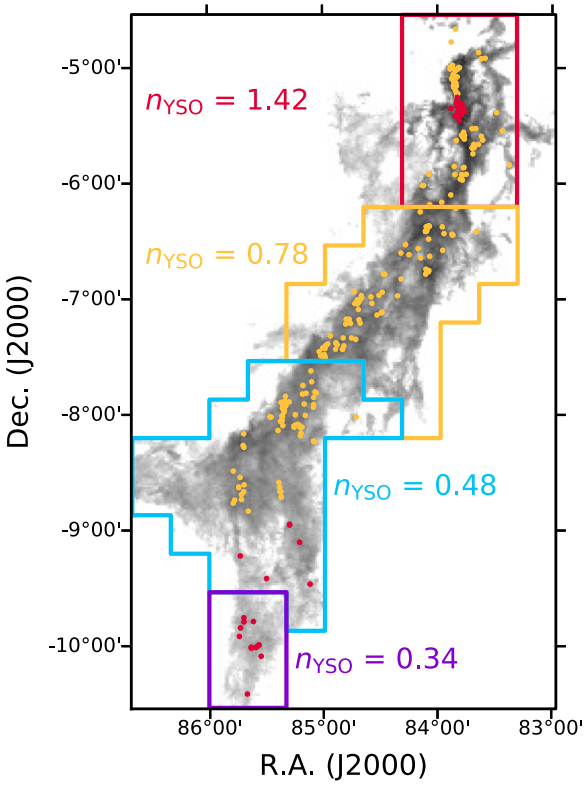

Figure 8. Positions of the Class 0/I YSOs and flat-spectrum sources (the embedded protostars) in the Orion A cloud. The background image presents the integrated intensity map of the ^{13}CO line. The embedded protostars identified with Herschel observations (Furlan et al. 2016) are represented by the yellow dots. Because Furlan et al. (2016) missed protostars near the Orion nebular and L1647, the YSO catalog identified using the Spitzer Space Telescope (Megeath et al. 2012) is adopted for these regions (red dots). The number density of the embedded protostars (n_{YSO}) for each subregion is summarized on the map. The unit of n_{YSO} is per square parsec.

Table 6
Distribution of the Embedded Protostars

Region	N_{YSO}	Area[a] (pc^2)	n_{YSO} (pc^{-2})	Total L_{bol}[b] ($L_\odot$)
In the Orion A cloud				
ISF	111	78.0	1.42	973.9
Tail-N	88	113.2	0.78	722.0
Tail-S	78	163.5	0.48	106.1
L1647-S	15	43.7	0.34	···
In the Ophiuchus cloud				
L1688	50	6.0	8.32	59.2
L1709	4	6.3	0.63	2.6

Notes.
[a] For the Orion A cloud, we adopted the distances presented in Table 1 to derive the area for the subregions. For the Ophiuchus cloud, the distance of 137 pc is adopted (Ortiz-León et al. 2017).
[b] The total bolometric luminosities for the subregions in the Orion A and Ophiuchus clouds are derived from the YSO catalogs provided by Furlan et al. (2016) and Dunham et al. (2015), respectively. Note that the protostars near OMC-1 and L1647 are not included in the catalogs.

L_{bol} also decreases in the subregions from the north to the south.

We also investigated the n_{YSO} and total L_{bol} for the L1688 and L1709 regions. The Spitzer YSO catalog produced by Dunham et al. (2015) was adopted to investigate the distribution of YSOs in the Ophiuchus cloud (see Figure 9 and Table 6). Similar to those for the Orion A cloud, both n_{YSO} and the total L_{bol} in the L1688 region are also higher than those for the L1709 region. Similar variation trends between the δv of the PCA scaling relations and the number density and total luminosity of the embedded protostars in the subregions imply that the turbulent velocity difference is affected by the local star formation activities.

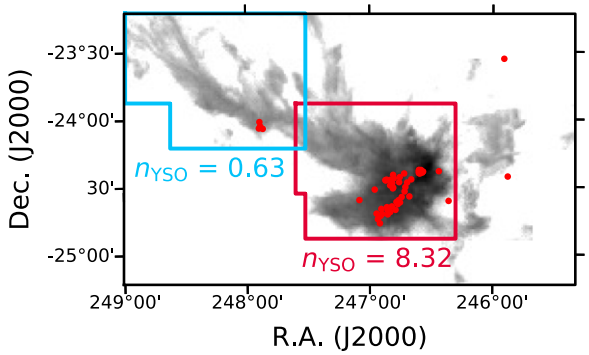

Figure 9. The same as Figure 8 but for the Ophiuchus cloud. The red dots represent the embedded protostars identified with Spitzer observations (Dunham et al. 2015).

Figure 7 shows that the δv for a given L also varies depending on the observed lines. At a certain L, the δv for C^{18}O, HCO$^+$, and CS are higher than that for ^{13}CO. The C^{18}O, HCO$^+$, and CS lines are optically thinner than the ^{13}CO line because of their lower abundances (Wilson & Rood 1994; Lee et al. 1998) or higher critical densities (Ungerechts et al. 1997). Consequently, these lines preferentially trace the dense environment compared to the ^{13}CO line. Therefore, the high-δv values for C^{18}O, HCO$^+$, and CS imply that the dense gas may be more turbulent than the diffuse gas in the ISF region. These results are remarkable because the high column density regions in both clouds have a broader ^{13}CO line width than the envelope regions. Also, the line width of ^{13}CO is generally broader than that of C^{18}O, HCO$^+$, and CS (Paper I).

Another important point is that the scaling relation for HCO$^+$ tends to have the largest δv in both clouds. This is likely because the HCO$^+$ line is mainly detected in the regions where stars actively form (Paper I). Shirley et al. (2003) derived the Type 2 (*single-tracer and multicloud*) line width-size relation using C^{34}S $J = 5-4$ for 51 high-mass star-forming cores. They found much broader line widths at a given size than those for the Type 1 (*multitracer and multicloud*) line width-size relations of *high-mass* and *low-mass* cores derived by Caselli & Myers (1995). Certain molecular transitions preferentially trace gas that is much more turbulent than gas in other parts of the cloud. However, our result that higher δvs are derived from higher density tracers requires some discussion because it is conventionally accepted that the turbulence dissipates in dense environments, thereby resulting in narrower line widths (Myers 1983; Goodman et al. 1998; Nakano 1998).

5.2. Effect of the Orion KL Outflows on the PCA

In the ISF, there are energetic features that originate from active star formation such as high-velocity outflows from Orion KL in OMC-1. Broad wing structures, produced by the Orion KL outflows, clearly appear in the ^{13}CO, HCO$^+$, and CS lines, and marginally in the C^{18}O line (Paper I). High-velocity outflows may provide the key to understanding the PCA results

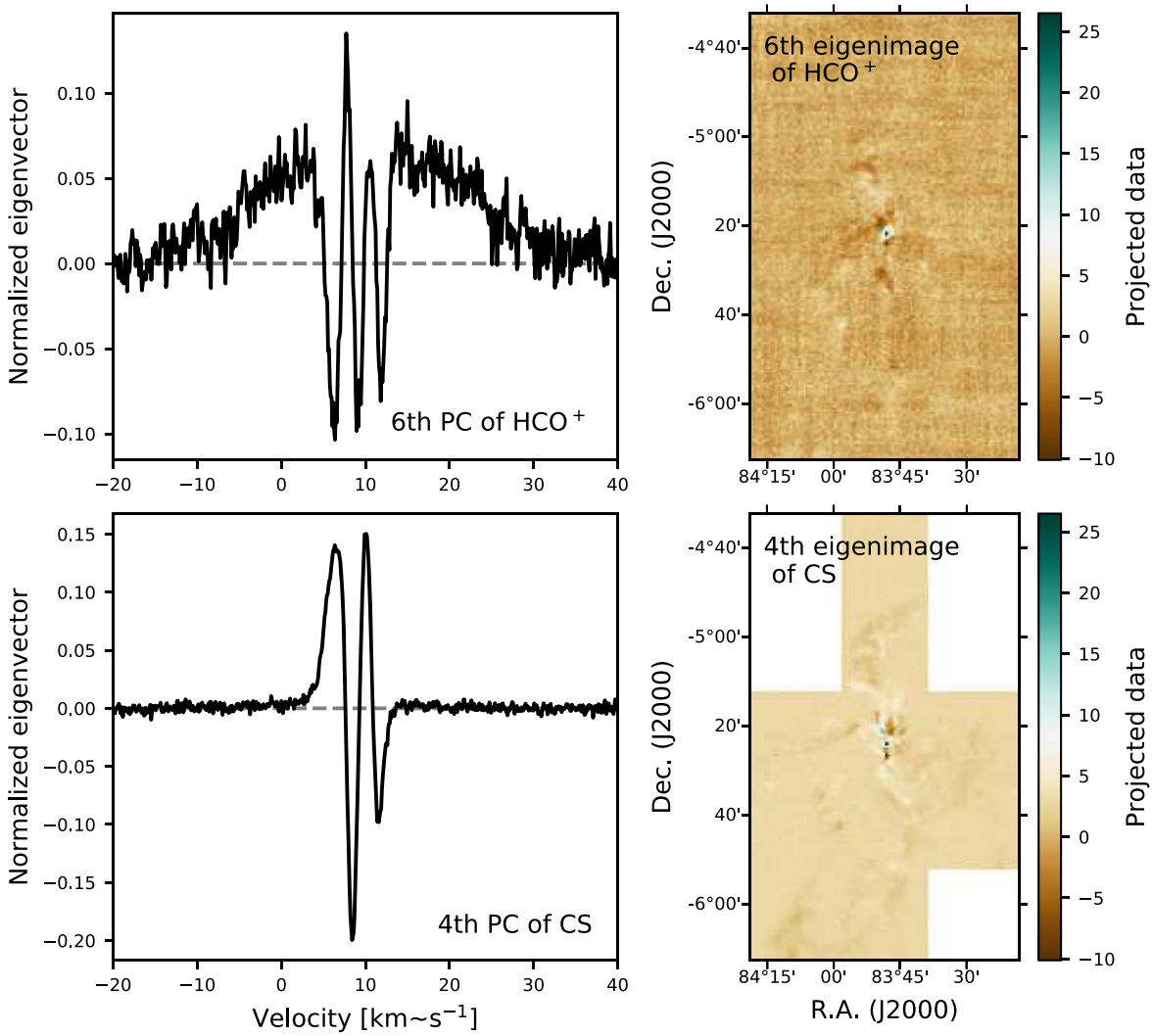

Figure 10. Eigenvectors (left) and eigenimages (right) for the PCs that are affected by the Orion KL outflows. The eigenvector and eigenimage for the 6th PC of HCO^+ are presented in the top panels, and those for the 4th PC of CS are presented in the bottom panels.

derived from the ^{13}CO maps, where we find δv varies with the n_{YSO} and total L_{bol} of the subregion (see Section 5.1).

The scaling relations for the observed lines in the ISF region show that there are two PCs that have high-δv values at a given L compared to the other PCs (see the black dashed boxes in Figure 7): one is the 6th PC of HCO^+ and the other is the 4th PC of CS. Figure 10 shows the eigenvectors and eigenimages of the 6th PC of HCO^+ and the 4th PC of CS. The HCO^+ eigenvector exhibits high-velocity wing structures that extend from -20 to 35 km s^{-1}. Its eigenimage also shows a large positive projection near Orion KL, which indicates that this component mainly describes a velocity difference near Orion KL. These features imply that the high δv of the 6th PC of HCO^+ probably originates from the Orion KL outflows, and the localized star formation activities increase the δv value of a specific PC. For the CS line, the eigenvector does not clearly show the broad wing structures, although its eigenimage presents large positive and negative projection values near Orion KL. These features may be due to the weak intensities of the broad wing structures compared to those for the HCO^+ line (Paper I).

We derived the scaling relations for the observed lines in the ISF excluding the spectra affected by the Orion KL outflows from the PCA. Since the outflow features are only detected near Orion KL, we can exclude the outflow contamination by removing the line spectra within a circular area that is centered at Orion KL ($\alpha_{J2000} = 5^h35^m14.16^s$, $\delta_{J2000} = -5°22^m21.5^s$) with a diameter of 5′. Figure 11 shows the scaling relations without the Orion KL outflows. In these scaling relations, the PCs with the high-δv values (the 5th PC of HCO^+ and 3rd PC of CS in the original results; see Figure 7) disappear. This result confirms that the Orion KL outflows do indeed enhance the δv values of the 6th PC of HCO^+ and the 4th PC of CS.

5.3. Steep Slope and Low δv of ^{13}CO in the ISF

The scaling relation for ^{13}CO in the ISF region has a higher α than those for the other subregions (see Figure 6). This steep slope does not appear to be caused by the Orion KL outflows because it still appears in the scaling relation after the Orion KL region is removed (see Figure 11). The large α could be attributed to a steep increase in δv at L of about 0.3 pc.

We mask the inner area of the ISF region, where the HCO^+ line is detected over 5σ, from the ^{13}CO map (see the pink contour in Figure 12) to assess the origin of the high-δv values at $L \geqq 0.3$ pc. The PCA result for the masked ^{13}CO data (the pink squares) represents the gas motion in the remaining

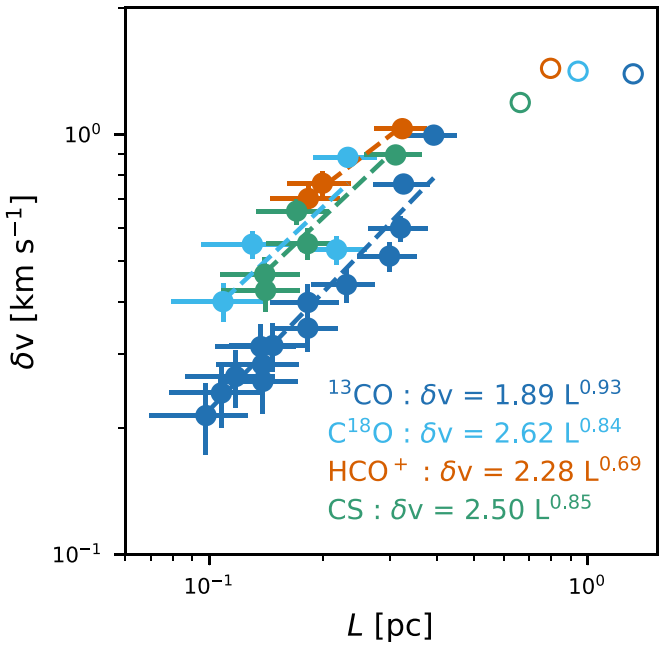

Figure 11. The scaling relations for the ^{13}CO, C^{18}O, HCO$^+$, and CS lines in the ISF region after excluding the Orion KL outflows. The PCA results are derived from the ISF region except near Orion KL (a circular area centered on Orion KL with a diameter of 5′).

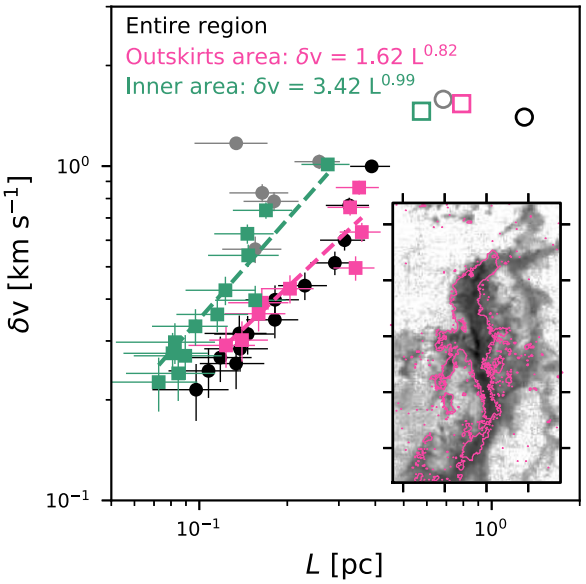

Figure 12. The scaling relation for the ^{13}CO line in the outskirts (the pink squares) and inner area (the green squares) of the ISF region. The boundary of the outskirts and inner areas (the pink contour) is defined where the HCO$^+$ line is detected over the 5σ level. The original scaling relations for ^{13}CO (the black circles) and HCO$^+$ (the gray circles) are also overlaid for a comparison.

outskirts of the ISF. Figure 12 shows that the drastic change in δv at $L \sim 0.3$ pc still exists. This velocity excess could still be related to the Orion KL outflow if it is produced by turbulence excited by the outflow expansion. Offner & Liu (2018) and Offner & Chaban (2017) showed that stellar winds and outflows can excite magnetosonic waves, which propagate away from where the feedback is launched, thereby enhancing turbulence in regions removed from where the feedback is produced. Alternatively, the steep increase in δv at $L \geqq 0.3$ pc could be caused by large-scale motion of the filamentary structure rather than by local star formation activity, such as outflows and jets.

We also apply the PCA to the inner area of the ^{13}CO map (the green squares), where the HCO$^+$ line is detected. The derived scaling relation shows velocity differences greater than those derived from only the outskirt area. However, they are as large as those derived from the HCO$^+$ map (the gray circles). This result implies that the ^{13}CO line also traces the gas affected by the active star formation in ISF as the HCO$^+$ line does. However, in the PCA for the entire ISF region, these high-δv values of the inner area would be diluted because of the contribution of the outskirts.

5.4. Large-scale Motion of the ISF

Large-scale systematic motion, such as rotation and shear, affects the PCA result, and thus, we should consider its effect to determine the properties of turbulence (Burkert & Bodenheimer 2000; Federrath et al. 2016). The steep increase in δv at 0.3 pc, which was discussed in Section 5.3, probably results from a large-scale velocity gradient across the ISF. Therefore, we subtract the large-scale motion from the original velocity field to check the effect of the outskirts of the ISF on the PCA (see magenta symbols in Figure 12).

Federrath et al. (2016) subtracted the large-scale systematic motion of the central molecular zone cloud to obtain the velocity distribution function of turbulence. They fit the intensity weighted velocity (moment 1) map with a plane to isolate the systematic velocity gradient of the cloud from the turbulent velocity field. We apply the same method to the ^{13}CO data of the ISF. We fit the moment 1 map of the ISF, which is adopted from Paper I, with a plane. Subsequently, the fitted velocity gradient across the ISF is subtracted from the original ^{13}CO cube data (see Figure 13).

Figure 14 presents the PCA results after the subtraction of the systematic velocity gradient. The steep increase of δv disappears after the velocity gradient was subtracted (the gray dashed box). Also, all (δv, L) points are well aligned and can be well fit with a single power law. When we apply the PCA to the entire ISF region, the α value decreases from 0.93–0.76 after the subtraction. These results strongly suggest that the steep increase in δv originates from the large-scale motion of the ISF.

6. Summary

To study the relation between turbulence and star formation in molecular clouds, we observed the Orion A and Ophiuchus clouds in six different molecular lines as one of TRAO-KSPs, TIMES (Paper I). We investigated the properties of turbulence traced by ^{13}CO $J = 1$–0, C^{18}O $J = 1$–0, HCO$^+$ $J = 1$–0, and CS $J = 2$–1 by applying a statistical method, PCA. The main results of the analyses are summarized as follows:

1. The uniform distribution of $T_{\rm rms}$ allows us to access the gas motion on small scales using PCA.
2. For the entire Orion A and Ophiuchus clouds, PCA scaling relations for the ^{13}CO line have α and δv_0 values that are consistent with those of the universality of turbulence proposed by Heyer & Brunt (2004).
3. When we apply PCA to the ^{13}CO data in the subregions of the Orion A and Ophiuchus clouds, the δv for a given L varies depending on the subregions. In each cloud, the δv for a given L is generally higher in subregions that are more actively star forming.

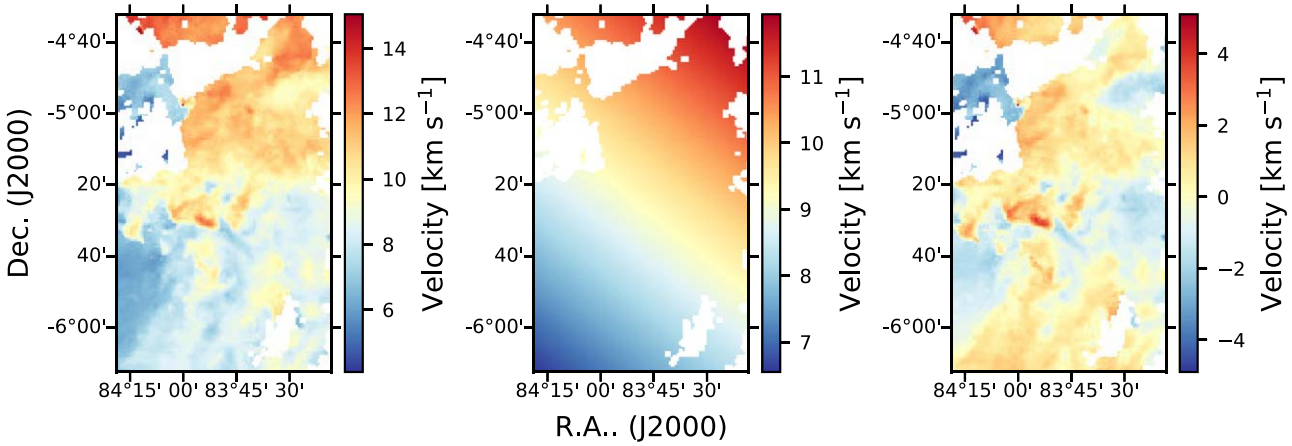

Figure 13. Left panel: intensity weighted velocity (moment 1) map of the ^{13}CO line in the ISF region (Paper I). Middle panel: large-scale velocity gradient in the ISF region. The large-scale gradient is isolated from the turbulent velocity field via fitting the moment 1 map with a plane. Right panel: moment 1 map for the remaining turbulent velocity field.

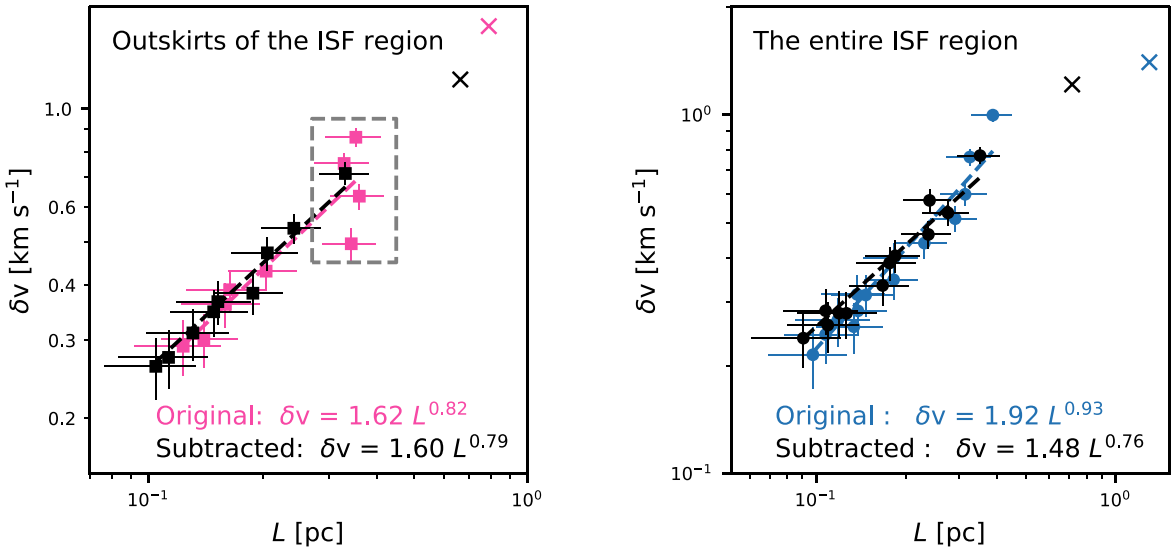

Figure 14. The scaling relations for the ^{13}CO line in the outskirts (left panel) and entire ISF region (right panel) after the subtraction of the large-scale velocity gradient. In each panel, the scaling relation for the original data is overlaid for comparison. The gray dashed box in the left panel indicates the steep increase in δv at 0.3 pc.

4. The variation in δv is related to the $n_{\rm YSO}$ and total $L_{\rm bol}$ of the subregions. Meanwhile, localized phenomena, such as the Orion KL outflows, can change the δv of a specific PC.
5. The scaling relations of the observed lines in the ISF and L1688 regions show that the δv of C^{18}O, HCO$^+$, and CS are generally higher than that of ^{13}CO. This implies that the dense gas is more turbulent than the diffuse gas in these regions, probably due to energy input from active star formation in the dense regions.
6. The scaling relation of the ^{13}CO line only in the dense inner part of the ISF shows δv similar to that derived from the HCO$^+$ line. However, this high δv would be diluted in the PCA of the entire ISF region because the scaling relation is more affected by the larger outskirt area.
7. The scaling relation for the ^{13}CO line in the ISF region has a steep increase in δv at L of about 0.3 pc, resulting in a large α. This increase in δv may be due to magnetosonic waves excited by Orion KL or due to large-scale motion of the filamentary cloud.

This work was supported by the National Research Foundation of Korea (NRF) grant funded by the Korean government (MSIT) (grant No. 2021R1A2C1011718). K.T. was supported by JSPS KAKENHI Grant No. 20H05645.

Appendix
The Selection of Significant PCs

One important factor in the PCA is the number of significant PCs ($N_{\rm sig}$) that cover most of the variation in the data (Jolliffe 2002). The scree plot method (Cattell 1966) is one of the standard methods to evaluate $N_{\rm sig}$ in multivariate statistics (Zoski & Jurs 1990; Jolliffe 2002; Kanyongo 2005). In this study, the significant PCs were selected by checking the variation of δv (see Section 3). Here, we apply the scree plot method to our PCA result for the ^{13}CO line in the Orion A cloud to check the reliability of our method.

The scree plot (Cattell 1966) is a plot of the eigenvalue (λ_i) against the order number (i). The scree plot can have elbow points, which separate the scree plot into two parts: *steep* and *shallow*, which are located on the left and right, respectively, of

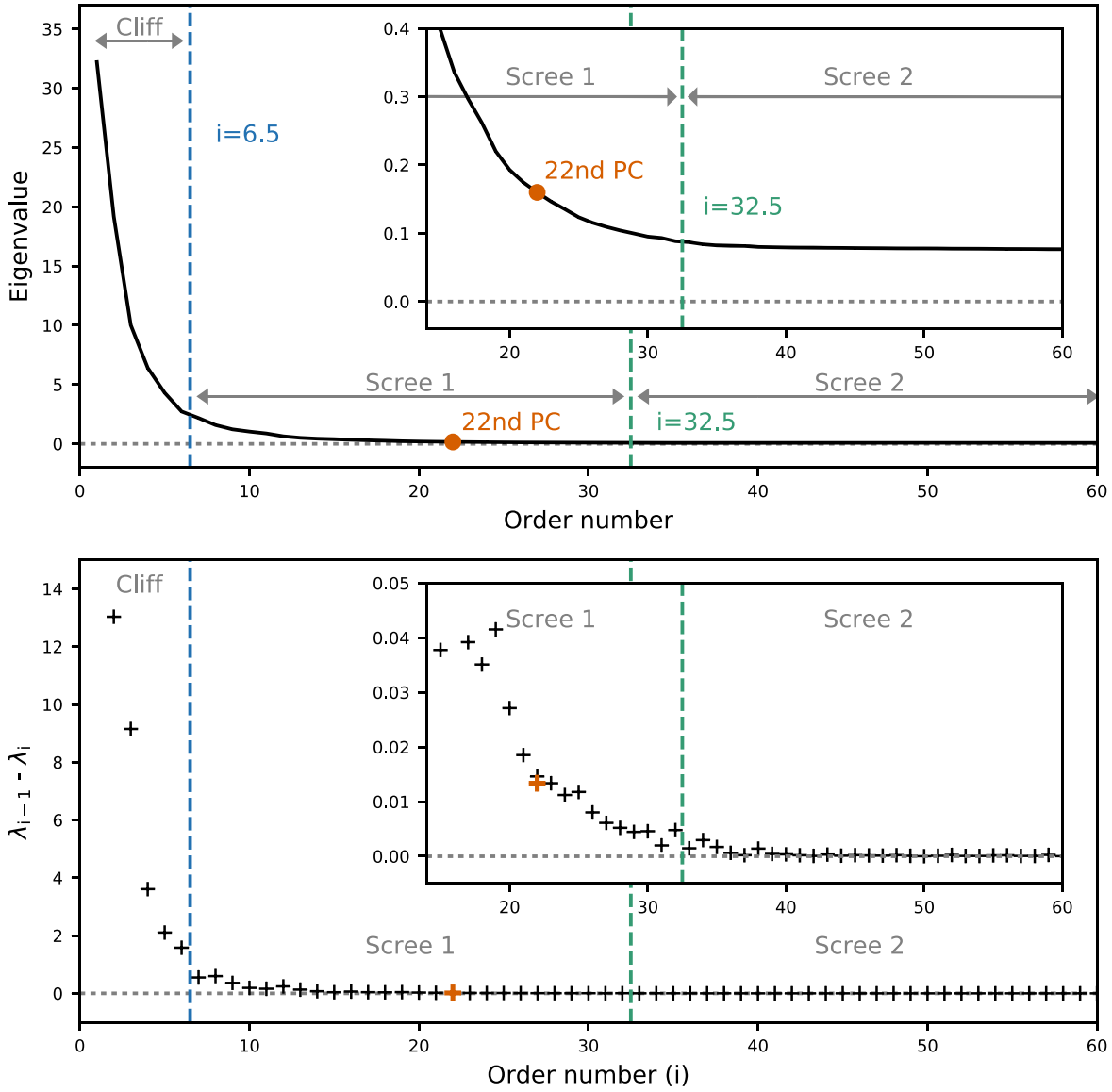

Figure A1. Scree plot (top) and the variation of eigenvalue (i.e., $\lambda_{i-1} - \lambda_i$) as a function of order number (bottom) for the ^{13}CO line in the Orion A cloud. The insets are the zoomed-in views for i from 14–60. The blue dashed lines indicate the boundary between the Cliff and Scree 1 regimes ($i = 6.5$), and the green dashed lines indicate the boundary between the Scree 1 and Scree 2 regimes ($i = 32.5$). The 22nd PC, which is the largest order PC selected by our method, is marked with the orange symbols.

each elbow point. If the scree plot has a single elbow point, the left and right of the elbow point are labeled as *Cliff* and *Scree*, respectively. It is possible to have multiple elbow points in a scree plot (Cattell 1966; Jolliffe 2002). In this case, the left of the first elbow point is the Cliff regime (Zoski & Jurs 1990; Kanyongo 2005). The PCs in the Cliff regime are considered significant in many studies (Cattell 1966; Zoski & Jurs 1990; Jolliffe 2002; Kanyongo 2005).

Figure A1 shows the scree plot for the ^{13}CO line in the Orion A cloud. We also present the variation of λ_i (i.e., $\lambda_{i-1} - \lambda_i$) as a function of i, which is frequently used as a criterion to identify significant PCs (Jolliffe 2002). The first elbow point is in between $i = 6$ and 7 (the blue dashed line) since $\lambda_{i-1} - \lambda_i$ remains relatively constant beyond the 6th PC (Jolliffe 2002). It is difficult to determine whether additional elbow points exist because the scree plot changes smoothly. We thus consider the left and right of the first elbow point as a Cliff and Scree regimes, respectively. The λ_i continuously decrease in the Scree regime up to the 32nd order. Beyond the 32nd PC, λ_i remains constant, and $\lambda_{i-1} - \lambda_i$ is close to zero. We thus divide the Scree regime by the 32nd PC into *Scree 1* and *Scree 2*; Scree 1 covers $i = 7$–32, and Scree 2 is beyond $i = 32$.

Surprisingly, $N_{\rm sig}$ from the scree plot is 6, which is much smaller than that from our method ($N_{\rm sig} = 22$; the orange symbols in Figure A1). The percentage of total variation ($p_{\rm var}$; see Equation (3)) for the PCs that were selected with the scree plot and our methods are 63% and 72%, respectively. If we consider all components within the Cliff and Scree 1 regimes (PCs from the 1st to 32nd), $p_{\rm var}$ is 73%, which is not significantly different from the result of our selection method. These results imply that the scree plot method is a more conservative method for evaluating $N_{\rm sig}$, but our method selects all PCs that are significant enough to describe the most variations caused by turbulence, limiting the effect of noise.

The left panel of Figure A2 shows the (δv, L) points of the PCs within the Cliff and Scree 1 regimes. Note that the 1st PC is omitted, and the 2nd PC is marked with the cross symbol as marked in Figure 1. We divide the PCs into three groups:

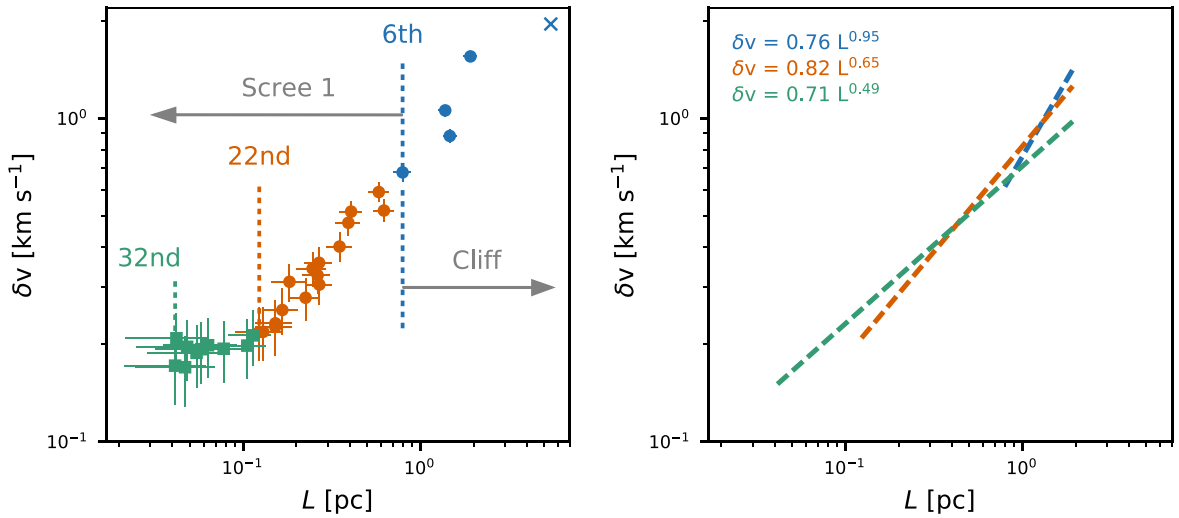

Figure A2. Left panel: the (δv, L) points for the PCs in the Cliff and Scree 1 regimes (up to the 32nd PC). The 1st PC is omitted, and the 2nd PC is represented by the blue cross symbol. The PCs within the three groups, which are divided by the 6th and the 22nd PCs (see the text), are exhibited in different colors. Right panel: the scaling relation for the PCs from the 3rd to the last component in each of the three groups. The best-fit relations are summarized in the upper-left corner.

(1) from the 3rd to the 6th (in the Cliff regime; the blue symbols), (2) from the 7th to the 22nd (the PCs in the Scree 1 regime and selected via our method; the orange symbols), and (3) from the 23rd to the 32nd (the rest of the PCs in the Scree 1 regime; the green symbols). The best-fit scaling relation for the (δv, L) points from the 3rd to the last component in each group is presented in the right panel of Figure A2. The $N_{\rm sig}$, $p_{\rm var}$, best-fit δv_0 and α values are summarized in Table A1.

Beyond the 22nd PC, δv converges into about 0.2 km s^{-1}, and consequently α decreases as more PCs are included in the power-law fitting. The eigenvector and eigenimage of the last-order PC in each group (the 6th, 22nd, and 32nd PCs) are presented in Figure A3. The noise contamination of the eigenvector and eigenimage becomes more significant as i increases. This contamination probably results in the convergence of δv beyond the 22nd PC.

The PCs with L smaller than 0.8 pc are excluded from the scaling relation if we adopt $N_{\rm sig}$ determined only by the scree plot method. Therefore, we cannot assess turbulence on small scales. The uncertainty of α is also large since only four PCs are included in the fitting process (see Table A1). In addition, our method covers the largest percentage of the total variation while avoiding noise contamination because the PCs beyond the 22nd PC are significantly affected by noise, as presented in Figure A3. These results imply that our method is more appropriate to constrain $N_{\rm sig}$, and thus, more precise properties of turbulence.

Table A1
The PCA Results with Different $N_{\rm sig}$

Included PCs	$N_{\rm sig}$	$p_{\rm var}$	$\log_{10}(\delta v_0)$	α
Cliff	6	63.2	-0.12 ± 0.04	0.95 ± 0.20
Orion A[a]	22	72.1	-0.09 ± 0.02	0.65 ± 0.05
Cliff & Scree 1	32	73.0	-0.15 ± 0.03	0.49 ± 0.06

Note.
[a] The result for the PCs selected via our method. The values are the same as that presented in Table 3.

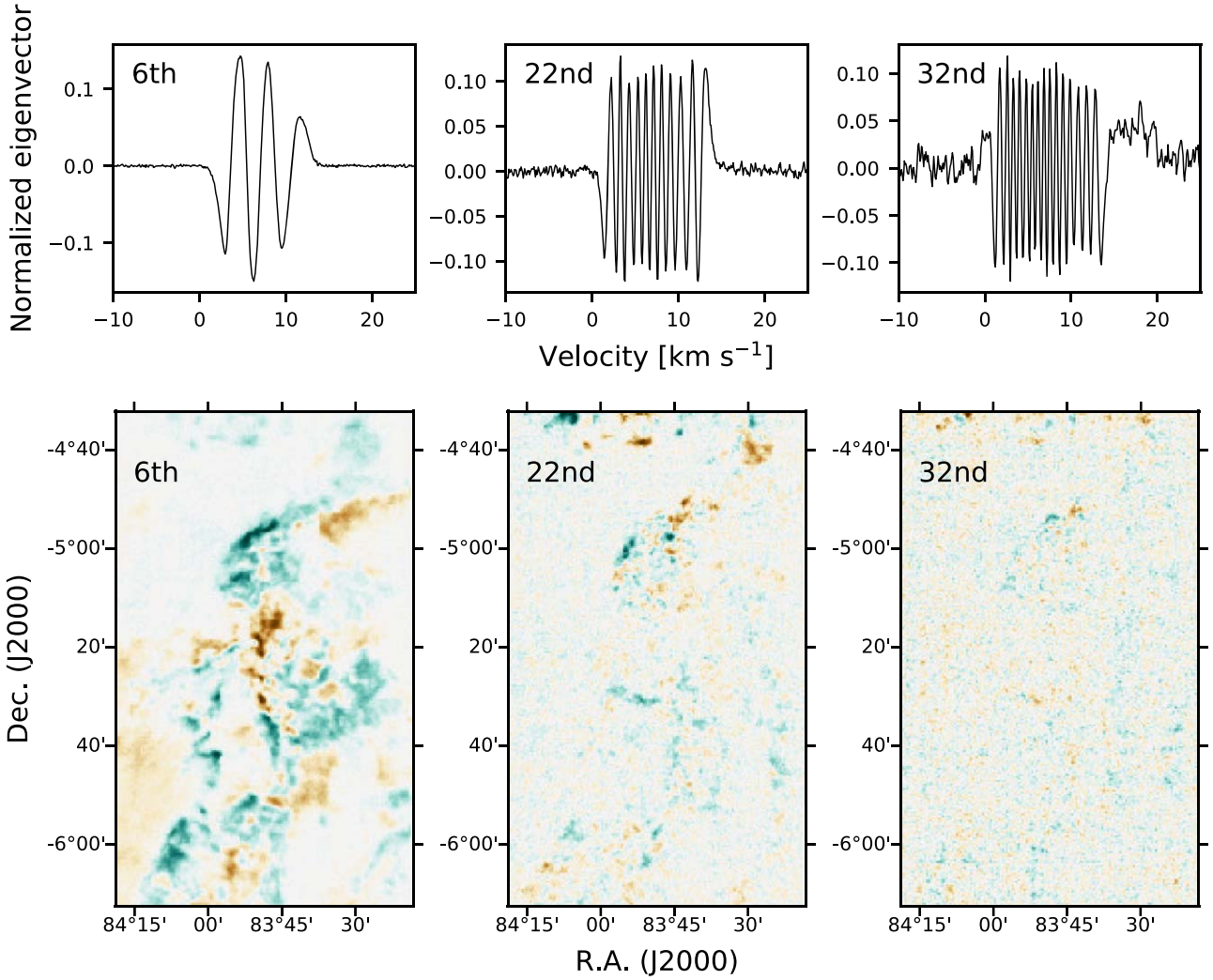

Figure A3. Eigenvectors (top) and eigenimages (bottom) for the last component in each of the three groups defined in the Appendix.

ORCID iDs

Hyeong-Sik Yun https://orcid.org/0000-0001-6842-1555
Jeong-Eun Lee https://orcid.org/0000-0003-3119-2087
Neal J. Evans, II https://orcid.org/0000-0001-5175-1777
Stella S. R. Offner https://orcid.org/0000-0003-1252-9916
Mark H. Heyer https://orcid.org/0000-0002-3871-010X
Jungyeon Cho https://orcid.org/0000-0003-1725-4376
Brandt A. L. Gaches https://orcid.org/0000-0003-4224-6829
Yao-Lun Yang https://orcid.org/0000-0001-8227-2816
How-Huan Chen https://orcid.org/0000-0001-6222-1712
Yunhee Choi https://orcid.org/0000-0002-3895-6169
Yong-Hee Lee https://orcid.org/0000-0001-6047-701X
Giseon Baek https://orcid.org/0000-0002-2814-1978
Jongsoo Kim https://orcid.org/0000-0002-1229-0426
Hyunwoo Kang https://orcid.org/0000-0001-9317-7646
Seokho Lee https://orcid.org/0000-0002-0226-9295
Ken'ichi Tatematsu https://orcid.org/0000-0002-8149-8546

References

Allen, L. E., & Davis, C. J. 2008, in Handbook of Star Forming Regions, ed. B. Reipurth, Vol. I (San Francisco: Astronomical Society of the Pacific), 621
Bally, J., Langer, W. D., Stark, A. A., & Wilson, R. W. 1987, ApJL, 312, L45
Boyden, R. D., Koch, E. W., Rosolowsky, E. W., & Offner, S. S. R. 2016, ApJ, 833, 233
Boyden, R. D., Offner, S. S. R., Koch, E. W., & Rosolowsky, E. W. 2018, ApJ, 860, 157
Brunt, C. M. 1999, PhD thesis, Univ. Massachusetts
Brunt, C. M., & Heyer, M. H. 2002a, ApJ, 566, 289
Brunt, C. M., & Heyer, M. H. 2002b, ApJ, 566, 276
Brunt, C. M., & Heyer, M. H. 2013, MNRAS, 433, 117
Brunt, C. M., Heyer, M. H., Vázquez-Semadeni, E., & Pichardo, B. 2003, ApJ, 595, 824
Burkert, A., & Bodenheimer, P. 2000, ApJ, 543, 822
Caselli, P., & Myers, P. C. 1995, ApJ, 446, 665
Cattell, R. 1966, Multivariate Behav. Res., 1, 245
Dunham, M. M., Allen, L. E., Evans, N. J., II, et al. 2015, ApJS, 220, 11
Elmegreen, B. G., & Scalo, J. 2004, ARA&A, 42, 211
Feddersen, J. R., Arce, H. G., Kong, S., Ossenkopf-Okada, V., & Carpenter, J. M. 2019, ApJ, 875, 162
Federrath, C. 2015, MNRAS, 450, 4035
Federrath, C. 2018, PhT, 71, 38
Federrath, C., & Klessen, R. S. 2012, ApJ, 761, 156
Federrath, C., Klessen, R. S., Iapichino, L., & Beattie, J. R. 2021, NatAs, 5, 365
Federrath, C., Rathborne, J. M., Longmore, S. N., et al. 2016, ApJ, 832, 143
Furlan, E., Fischer, W. J., Ali, B., et al. 2016, ApJS, 224, 5
Gaches, B. A. L., Offner, S. S. R., Rosolowsky, E. W., & Bisbas, T. G. 2015, ApJ, 799, 235
Gammie, C. F., & Ostriker, E. C. 1996, ApJ, 466, 814
Goodman, A. A., Barranco, J. A., Wilner, D. J., & Heyer, M. H. 1998, ApJ, 504, 223
Grellmann, R., Preibisch, T., Ratzka, T., et al. 2013, A&A, 550, A82

Großschedl, J. E., Alves, J., Meingast, S., et al. 2018, A&A, 619, A106
Hennebelle, P., & Falgarone, E. 2012, A&ARv, 20, 55
Heyer, M., Krawczyk, C., Duval, J., & Jackson, J. M. 2009, ApJ, 699, 1092
Heyer, M. H., & Brunt, C. M. 2004, ApJL, 615, L45
Heyer, M. H., Morgan, J., Schloerb, F. P., Snell, R. L., & Goldsmith, P. F. 1992, ApJL, 395, L99
Heyer, M. H., & Schloerb, F. P. 1997, ApJ, 475, 173
Heyer, M. H., Williams, J. P., & Brunt, C. M. 2006, ApJ, 643, 956
Ikeda, N., Sunada, K., & Kitamura, Y. 2007, ApJ, 665, 1194
Jeong, I.-G., Kang, H., Jung, J., et al. 2019, JKAS, 52, 227
Jolliffe, I. T. 2002, Principal Component Analysis (New York: Springer),
Kanyongo, G. 2005, JMASM, 4, 13
Klessen, R. S. 2000, ApJ, 535, 869
Klessen, R. S. 2004, Ap&SS, 292, 215
Koch, E. W., Ward, C. G., Offner, S., Loeppky, J. L., & Rosolowsky, E. W. 2017, MNRAS, 471, 1506
Kolmogorov, A. 1941, DoSSR, 30, 301
Kong, S., Arce, H. G., Feddersen, J. R., et al. 2018, ApJS, 236, 25
Kounkel, M., Covey, K., Suárez, G., et al. 2018, AJ, 156, 84
Larson, R. B. 1981, MNRAS, 194, 809
Lee, H.-H., Roueff, E., Pineau des Forets, G., et al. 1998, A&A, 334, 1047
Loren, R. B. 1989, ApJ, 338, 925
Mac Low, M. M. 2003, in Turbulence and Magnetic Fields in Astrophysics, ed. E. Falgarone & T. Passot, Vol. 614 (Berlin: Springer), 182
Mac Low, M.-M., & Klessen, R. S. 2004, RvMP, 76, 125
McKee, C. F., & Ostriker, E. C. 2007, ARA&A, 45, 565
Megeath, S. T., Gutermuth, R., Muzerolle, J., et al. 2012, AJ, 144, 192
Motte, F., Andre, P., & Neri, R. 1998, A&A, 336, 150
Myers, P. C. 1983, ApJ, 270, 105
Nagahama, T., Mizuno, A., Ogawa, H., & Fukui, Y. 1998, AJ, 116, 336
Nakamura, F., Miura, T., Kitamura, Y., et al. 2012, ApJ, 746, 25
Nakano, T. 1998, ApJ, 494, 587
Offner, S. S. R., & Chaban, J. 2017, ApJ, 847, 104
Offner, S. S. R., & Liu, Y. 2018, NatAs, 2, 896
Ortiz-León, G. N., Loinard, L., Kounkel, M. A., et al. 2017, ApJ, 834, 141
Ossenkopf, V., & Mac Low, M. M. 2002, A&A, 390, 307
Padoan, P., Federrath, C., Chabrier, G., et al. 2014, in Protostars and Planets VI, ed. H. Beuther et al. (Tucson: Univ. Arizona Press), 77
Padoan, P., Juvela, M., Goodman, A. A., & Nordlund, Å. 2001, ApJ, 553, 227
Passot, T., Pouquet, A., & Woodward, P. 1988, A&A, 197, 228
Ridge, N. A., Di Francesco, J., Kirk, H., et al. 2006, AJ, 131, 2921
Roh, D.-G., & Jung, J. H. 1999, PKAS, 14, 123
Roman-Duval, J., Federrath, C., Brunt, C., et al. 2011, ApJ, 740, 120
Shimajiri, Y., Kawabe, R., Takakuwa, S., et al. 2011, PASJ, 63, 105
Shirley, Y. L., Evans, N. J. I., Young, K. E., Knez, C., & Jaffe, D. T. 2003, ApJS, 149, 375
Solomon, P. M., Rivolo, A. R., Barrett, J., & Yahil, A. 1987, ApJ, 319, 730
Tatematsu, K., Umemoto, T., Kameya, O., et al. 1993, ApJ, 404, 643
Ungerechts, H., Bergin, E. A., Goldsmith, P. F., et al. 1997, ApJ, 482, 245
Walch, S., Whitworth, A. P., & Girichidis, P. 2012, MNRAS, 419, 760
Wilking, B. A., Gagné, M., & Allen, L. E. 2008, in Handbook of Star Forming Regions, ed. B. Reipurth, Vol. II (San Francisco: Astronomical Society of the Pacific), 351
Wilson, T. L., & Rood, R. 1994, ARA&A, 32, 191
Xu, S. 2020, MNRAS, 492, 1044
Yun, H.-S., Lee, J.-E., Choi, Y., et al. 2021, ApJS, 256, 16
Zhang, M., & Wang, H. 2009, AJ, 138, 1830
Zoski, K., & Jurs, S. 1990, Eval. Rev., 14, 214
Zucker, C., Speagle, J. S., Schlafly, E. F., et al. 2019, ApJ, 879, 125